Materials Today Bio 1 (2019) 100003

Contents lists available at ScienceDirect

Materials Today Bio

journal homepage: www.journals.elsevier.com/materials-today-bio

Spatially resolved small-angle X-ray scattering for characterizing mechanoresponsive liposomes using microfluidics

Marzia Buscema [a], Hans Deyhle [a], Thomas Pfohl [a,b], Andreas Zumbuehl [c,d], Bert Müller [a,*]

[a] Biomaterials Science Center, Department of Biomedical Engineering, University of Basel, Gewerbestrasse 14, CH-4123 Basel, Switzerland
[b] Institute of Physics, University of Freiburg, Freiburg, Germany
[c] Department of Chemistry, University of Fribourg, Fribourg, Switzerland
[d] National Center of Competence in Research in Chemical Biology, Geneva, Switzerland

A B S T R A C T

Atherosclerosis gives rise to blood vessel occlusion associated with blood flow alteration and substantial increase of average wall shear stress. This modification was proved acting as a purely physical trigger for targeted vasodilator release from a particular type of liposomes composed of 1,3-diaminophospholipids (Pad-PC-Pad). The flow-induced structural changes of these faceted liposomes, however, are completely unknown. Therefore, spatially resolved small-angle X-ray scattering was combined with microfluidics to uniquely study the purely physical mechanisms, which give rise to the highly efficient drug release from mechanoresponsive liposomes of nanometer size. The microfluidic device, designed to mimic a stenotic blood vessel, consisted of a 1-mm-wide channel with a constriction, 125 μm in diameter. Here, the changes of the average bilayer thickness and the mean size of the mechanoresponsive liposomes have been locally detected under flow conditions. Overall shape and bilayer thickness do change already near the constriction inlet, but the alteration is dominant near the outlet. At a flow rate of 0.2 μL/s, the liposome's bilayer thickness increased by 30% compared to the situation well before the constriction and under static condition. The detected bilayer thickness increase of the faceted liposomes is in line with the mechanically induced loss of interdigitation between the phospholipid amide chains. These results imply that rather the gradient force than the wall shear stress provokes structural changes of Pad-PC-Pad liposomes and the related drug release at stenoses. The approach, i.e. the combination of microfluidics and spatially resolved small-angle X-ray scattering, paves the way to design highly efficient and specific systems for the targeted drug delivery at constrictions with predefined morphology.

1. Introduction

The local dysfunction of arteries can expose the patient to life-threatening situations, including myocardial infarction. Under these circumstances, the heart is insufficiently supplied with oxygen via coronary arteries. Here, the delivery of vasodilatory drugs is necessary and appropriate, although adverse effects have been reported [1]. Stenosed arteries have a drastically altered morphology with a cross-section reduction, which causes a substantial increase of the blood flow velocity and, as a consequence, gives rise to an increase of the average wall shear stress by at least one order of magnitude [2]. It has been proposed that this increased shear stress could be used as a purely physical trigger for targeted vasodilator delivery [3,4]. This study is based on liposomes because the Food and Drug Administration has approved these nano-containers for drug delivery. Nanometer-sized liposomes are powerful containers to entrap, transport, and deliver a wide variety of drugs in the human body [5,6]. The artificial 1,3-diaminophospholipid, Pad-PC-Pad [7], self-assembles in aqueous solution and can form faceted liposomes [3,8]. These liposomes are stable at rest and release their cargo at elevated shear stresses [3]. The mechanism behind, however, is hardly understood and was previously related to an attenuation of the defects in the contact lines between the facets of a vesicle [9].

Understanding how Pad-PC-Pad liposomes behave under dynamic conditions might support them as powerful drug delivery system. In fact, recent studies report that the adverse effects observed for bare and nitroglycerin-loaded Pad-PC-Pad liposomes *in vitro* and *in vivo* are comparable or even lower than for established liposomal formulations [10,11].

In order to quantitatively assess the structure of liposomes, many methods have been used, including nuclear magnetic resonance [12], dynamic light scattering (DLS) [13], cryogenic transmission electron microscopy (cryo-TEM) [14], atomic force microscopy (AFM) [15], and small-angle X-ray scattering (SAXS) and neutron scattering [16,17]. SAXS is of particular interest because this method gives access to numerous characteristic quantities of the liposomes in terms of shape, size, lamellarity, and bilayer thickness. Garcia et al. [16] have shown, for example, that SAXS allows not only for the determination of size but also for the structural dependence on the solvent used and the osmotic

* Corresponding author.
E-mail address: bert.mueller@unibas.ch (B. Müller).

https://doi.org/10.1016/j.mtbio.2019.100003
Received 15 November 2018; Received in revised form 18 March 2019; Accepted 23 March 2019
Available online 2 April 2019

shrinkage of a complex liposomal drug. SAXS, however, does not only enable to perform static measurements but also the combination with microfluidics permits dynamic studies [18], i.e. studies of the mechanoresponsive properties of non-spherical liposomes. Spatially resolved SAXS using synchrotron radiation [19] has been applied to visualize human tissues in two dimensions [20,21] and more recently even in three dimensions [22]. It has been also used to map soft matter within a flow field [23]. The payoff of combining microfluidics and SAXS can been seen for diverse examples. One can observe the mixing of fluids [24,25], the *in situ*, real-time changes of the structural properties of proteins [24,26], of DNA [27], of surfactant solutions [28], of polymers [29], of liquid crystals [30], of worm-like micelles [23], and of nanocapsules [31]. Poulos et al. have reported that under shear, the lamellar phases of highly concentrated complex surfactant solutions depend strongly on the fluid direction. Multilamellar phases, subjected to the identical flow fields, were insensitive to contraction–expansion flows [28]. The study, however, is limited to the flow field on the lamellar periodicity and does not include overall shape alterations.

N. Venugopal Menon et al. have proposed a three-dimensional microfluidic chip modeling stenotic blood vessels with different severities to investigate vascular inflammation and leukocyte–endothelial cell adhesion. However, the study does not give information on how the cell's structure modifies under flow conditions [32].

Herein, we examine how Pad-PC-Pad liposomes in low-concentration suspension respond to shear stress changes by tuning the flow conditions in a microfluidic device. The design of the device mimics constricted blood vessels. In this manner, the alterations of the shear stress in wide (healthy) and constricted (diseased) segments of the device (artery) can be simulated. It should be noted that three q-ranges, which include the size of the liposomes and of the bilayer thickness, were of specific interest. The q-range of the SAXS pattern covers two orders of magnitude. The two-dimensional (2D) data represent the modifications in the flow field as a function of the flow rate. Pad-PC-Pad phospholipids belong to a peculiar category because the gap between the tails is capacious. Therefore, contrary to typical liposomes such as 1,2-dipalmitoyl-*sn*-glycero-3-phosphatidylcholine (DPPC) liposomes, the Pad-PC-Pad membranes can exhibit interdigitated phospholipids [9,33] characterized by a short bilayer thickness d_{id}, see scheme in Fig. 1. The interdigitation gives rise to additional bonding and significantly increases the membrane stiffness. Even a relatively small mechanical force deforms the soft membrane of, for example, DPPC/1, 2-Distearoyl-sn-glycero-3-phosphoethanolamine-Poly(ethylene glycol) (DSPE-PEG)), but the much stiffer Pad-PC-Pad membrane will withstand a deformation. The disordered and defect-rich parts of the non-spherical Pad-PC-Pad liposomes, however, will be affected. One can plausibly hypothesize that even a relatively small force can induce structural modifications at the bilayer membrane of the non-spherical liposomes. The structural modifications of Pad-PC-Pad liposomes under dynamic conditions might be related to a loss of the interdigitation. Thus, we should not only investigate mechanically induced shape and size changes of the liposomes but also focus on the potential changes of the membrane thickness. The spatially resolved SAXS experiments give access to the entire nanometer range, which includes the size and shape of the liposomes as well as the mean distance between the phospholipid heads.

2. Materials and methods

2.1. Liposome preparation

Two phospholipids, the commercially available natural DPPC with 5% M DSPE-PEG2000 (Lipoid, Zug, Switzerland) and the 1,3-palmitoylamido-1,3-deoxy-*sn*-glycero-2-phosphatidylcholine (Pad-PC-Pad) synthesized according to the recently reported protocol [7], were used to prepare liposomes. Briefly, the liposomes were formulated via the standard thin-film method [34,35] and hydrated with ultrapure water. Each suspension obtained has a lipid content of 20 mg/mL, which corresponds to the highest concentration achievable using Pad-PC-Pad. The suspensions were freeze-thawed in a twelve-step series of liquid nitrogen cooling and water bath heating (60 °C). To obtain liposomes with a diameter of about 100 nm with a narrow size distribution, multiple barrel extrusions using Liposofast LF-50 (Avestin Inc., Canada) through track-edged polycarbonate filter membranes (Whatman Nuclepore, Sigma-Aldrich, Buchs, Switzerland) were applied. The pore sizes were reduced from 400 nm (five times) via 200 nm (five times) to 100 nm (15 times).

2.2. Liposome characterization

The lipid concentration of the two formulations was determined using the phosphate test [36]. Size and size distribution of the liposomes were quantified by means of DLS using a Delsa Nano C (Beckman Coulter, USA). DLS measurements were performed at a temperature of 25 °C, using two laser diodes working at a wavelength of 658 nm. The scattering angle was set to 165°. Cryo-TEM images of Pad-PC-Pad liposomal suspension were taken by mounting the liposomal suspension on glow-discharged holey carbon grids, quickly frozen by a Cryoplunge CP3 system (Gatan, USA), and transferred to a JEM2200FS transmission electron microscope (JEOL, Japan) using a Gatan626 cryo-holder. Cryo-TEM micrographs were recorded at an acceleration voltage of 200 kV at a magnification of 20,000, 4–8 μm under-focus, and a dose of 10 electrons/$Å^2$, using a F416 CMOS detector (TVIPS, Germany).

2.3. Microfluidic device fabrication

X-ray compatible microfluidic devices were prepared as reported previously [23]. Briefly, photolithography of SU-8 negative resist (Nano SU-8 100, MicroChem Corp., MA, USA) on Si wafers was used to fabricate the masters. A layer of 250 μm thick photoresist was exposed to UV light through a photomask with the microfluidic design and was afterwards developed. The microfluidic device design consisted of a horizontal channel of 1000 μm width with a 2000-μm-long constriction in the middle. Two designs were realized, with constriction widths of 125 and 250 μm. Polydimethylsiloxane (PDMS, Sylgard 184, Dow Corning Corp., Midland, USA) and crosslinker were mixed at a ratio of 10:1 to form flexible replica stamps. The liquid PDMS mixture was poured on the photolithographic master and cured overnight at a temperature of 80 °C. Afterwards, the PDMS stamp was peeled off from the master. Norland Optical Adhesive 81 (Norland Products Inc., Cranbury, USA) was poured on a polyimide film of a thickness of 25 μm (Goodfellow Corp., Cambridge, UK). PDMS stamp was placed on the NOA 81 coated polyimide film in order to imprint the microfluidic structure into the NOA 81 coat. After 1 min of exposure to UV light, $\lambda = 366$ nm, to crosslink NOA 81, the flexible PDMS stamp was peeled off. By using a puncher 0.75 mm in diameter, inlet and outlet holes were obtained. The microfluidic NOA 81/polyimide film was then sealed with a second polyimide film with a thickness of 25 μm.

2.4. SAXS measurements

The spatially resolved SAXS measurements were performed at the cSAXS beamline at the Swiss Light Source (PSI, Villigen, Switzerland). The X-ray beam was focused to 25 μm × 50 μm (vertical × horizontal) spot size at the specimen location, and the photon energy was set to 11.2 keV (λ=1.1 Å) and the sample-detector distance to 7.102 m, determined by the first scattering order of a silver behenate specimen. The scattering signal was recorded using the Pilatus 2 M detector [37] (pixel size: 172 μm × 172 μm). Dynamic spatially resolved SAXS measurements of the liposomal suspensions were performed using microfluidic device mounted on an aluminum/polyetheretherketone/aluminum sample holder.

2D scans were realized line-by-line by continuously moving the device in the horizontal direction, while the detector recorded the data in the burst mode. 48 (v) × 96 (h) points at step size 25 μm (v) × 50 μm (h)

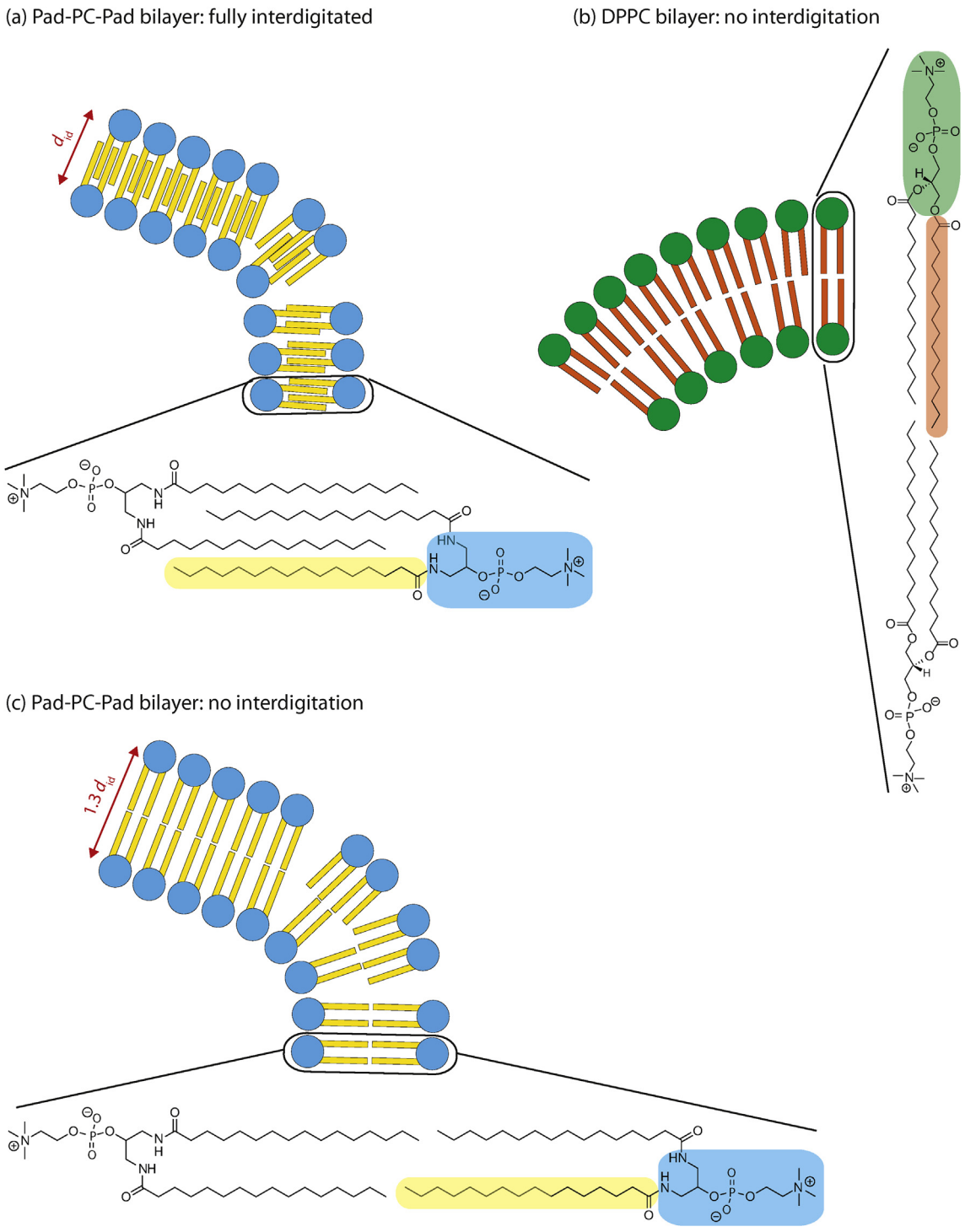

Fig. 1. Under static condition, the Pad-PC-Pad liposomes, derived from artificially synthesized lipids, show full interdigitation of the phospholipid tails (a), whereas DPPC liposomes based on natural lipids present no interdigitation of the bilayer (b). Under dynamic conditions, a loss of the bilayer interdigitation would give rise to an increased bilayer thickness by about 30% (c).

were acquired in a preselected region of the microfluidic device with an exposure time of 1.5 s per point. Thus, each 2D map was acquired in 1.92 h. The data were processed using the Matlab package available from the beamline (https://www.psi.ch/sls/csaxs/software). During the experiment, the flow rates were adjusted using a syringe pump system (Nemesys, Cetoni GmbH, Korbussen, Germany) connected to the microchannel using polytetrafluoroethylene (PTFE) tubing. For each flow rate investigated, one complete scan of the device was performed. As the same microfluidic device was used for both Pad-PC-Pad and DPPC/DSPE-PEG liposomes, prior to changing the type of liposome, the microfluidic device was flushed with water for more than 30 min. For the point-wise background correction, the scattering signal of ultrapure water in the microfluidic device for all the measured flow rates was recorded before the acquisition of the SAXS signal of the liposomal suspensions; the same exposure time and number of points used to scan the liposomal suspension were set for the acquisition of the scattering signal of water. For the microfluidic device with a rectangular channel cross section, the wall shear rates γ were calculated from the volumetric flow rates v using the

following equation [31]:

$$\gamma = 6v/h^2w \quad (1)$$

with γ the shear rate [s^{-1}], v the volumetric flow rate [μL/s], and w and h the width and height [μm] of the channel, respectively.

In addition, static SAXS measurements of the two liposomal suspensions and the ultrapure water were carried out in boron silicate glass capillaries (Hilgenberg, Malsfeld, Germany) having an outer diameter of 1.5 mm and wall thickness of 0.01 mm. These measurements also served for the evaluation of the X-ray beam and the sample-detector distance. Ten points, along the long axis of the capillary, were measured each with an exposure time of 1 s, followed by a rest period of 0.1 s.

3. Results and discussion

3.1. Liposome characterization

The final concentration of Pad-PC-Pad liposomes was (19.6 ± 1.3) mg/mL, whereas that of DPPC/DSPE-PEG was (20.2 ± 6.5) mg/mL.

The DLS results showed a mean diameter of (131.6 ± 0.9) nm for Pad-PC-Pad and a polydispersity index (PDI) of (0.103 ± 0.009), whereas for DPPC/DSPE-PEG, a mean diameter of (101.3 ± 0.5) nm and PDI of (0.256 ± 0.005) was found.

The cryo-TEM micrograph in Fig. 2 shows the morphology of Pad-PC-Pad, characterized by faceted and lentil-like shape [3,9]. The overall diameter appears to be in the range 100-200 nm, in agreement with DLS. The presence of round liposomes can be linked to the projective nature of cryo-TEM, as lenticular shapes seen top-on or slightly tilted will appear round. Nevertheless, the presence of spherical liposomes cannot be excluded.

3.2. SAXS measurement under static condition

The investigated q-range between 0.02 and 1.65 nm^{-1} corresponds to real-space distances d between 314 and 3 nm and, therefore, covers almost the entire nanometer range relevant for the characterization of the liposomes. The diagrams in Fig. 3 show the radially integrated scattering signal of DPPC/DSPE-PEG (top panel) and Pad-PC-Pad (bottom panel) liposomes acquired in suitable glass capillaries.

For DPPC/DSPE-PEG, the intensity peak at around 1.1 nm^{-1}, corresponding to 5.7 nm in real space, relates to the bilayer thickness.

For Pad-PC-Pad, the peak related to bilayer thickness is located at the edge of the detectable q-range, which additionally incurs into increased noise and thus cannot be unequivocally characterized.

Suitable models are often utilized in the interpretation of the scattering signal of the system investigated [38]. Herein, the scattering curves of DPPC/DSPE-PEG and Pad-PC-Pad were both fitted using a decoupling approach, which allowed factorization of the total form factor as product of a cross-section term for long dimension and a cross-section term for shorter dimension [39]. To fit the form factor related to the overall shape of DPPC/DSPE-PEG, a thin spherical shell model was used [40], whereas the intensity peak related to the bilayer was fitted using a function for a bilayer with a Gaussian electron density profile [41,42]. The model utilized to fit the bilayer provided the mean bilayer thickness $d_{DPPC/DSPE-PEG}$ between the two phospholipid heads and the standard deviation over the phospholipid heads.

To account for the polydispersity, the radii R and the $d_{DPPC/DSPE-PEG}$ were assumed to be normally distributed with means $R = 44.6$ nm and $d_{DPPC/DSPE-PEG} = 2.4$ nm.

The DPPC/DSPE-PEG liposomes mean diameter of 89.2 nm is smaller than the mean value obtained from the DLS (101.3 nm). It has been reported that DLS provides values up to 20% higher compared to SAXS as in SAXS solvent contrast variation does not allow detection of the hydrodynamic size of PEG bound to the liposomes surface [16]. As displayed in Fig. 3, the drop in intensity of the scattering curve of DPPC/DSPE-PEG at

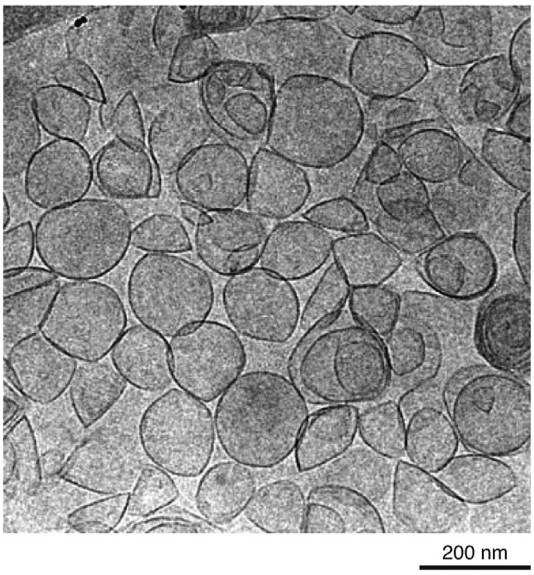

Fig. 2. Cryo-TEM micrograph of Pad-PC-Pad showing faceted liposomes with a size between 100 and 200 nm. The liposomes exhibit a wide variety of shapes. Cryo-TEM, cryogenic transmission electron microscopy.

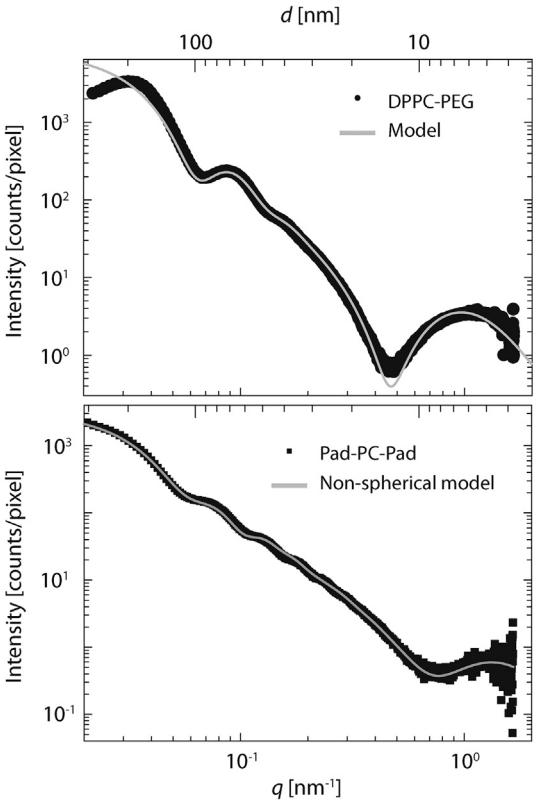

Fig. 3. Integrated scattering signals of DPPC/DSPE-PEG (black dots, top diagram) and Pad-PC-Pad (black squares, bottom diagram) under static condition. The DPPC/DSPE-PEG signal was fitted with a thin spherical shell model and a bilayer Gauss electron density profile model (grey line, top panel) with bilayer thickness $d_{DPPC/DSPE-PEG} = 2.4$ nm and $2\sigma = 3.0$ nm over the two phospholipid heads. Pad-PC-Pad scattering signal was fitted with a thin ellipsoidal shell model and a bilayer Gauss electron density profile model (grey line, bottom panel) with eccentricity ε of 0.43, interdigitated bilayer thickness of $d_{id} = 3.3$ nm and $2\sigma = 1.4$ nm over the two phospholipid heads. DPPC, 1,2-dipalmitoyl-*sn*-glycero-3-phosphatidylcholine.

the lowest q-values is attributed to interparticle interference [43]. The addition of PEG was reported to prevent liposome aggregation [44], i.e. providing for a repulsive interaction between the particles. In the model utilized, PEG contribution was not included.

The mean bilayer thickness $d_{DPPC/DSPE-PEG} = 2.4$ nm found for DPPC/DSPE-PEG is in line with the bilayer thickness value of 5.6 nm reported in

Table 1
Pad-PC-Pad liposome mean bilayer thickness under static condition (glass capillary) and under dynamic conditions in the seven regions (see sketch of Fig. 5) of the microfluidic device.

Flow rate[μL/s]	Glass capillary	Mean bilayer thickness [nm]						
		Microfluidic device positions						
		#1	#2	A	#3	B	#4	#5
0	3.3±0.8							
0.002		3.4±0.7	3.1±0.4	3.4±0.5	3.9±0.7	4.0±0.6	3.9±0.4	3.8±0.3
0.02		3.4±0.7	2.9±0.2	2.9±0.2	3.5±0.6	4.3±0.5	3.6±0.3	3.9±0.4
0.20		3.4±0.9	3.4±0.7	3.2±0.6	3.8±0.8	4.4±0.4	4.0±0.6	4.0±0.7

The data represent the mean values of the normal distribution, including the associated errors derived from the standard deviation.

Table 2
Radius of gyration R_g of Pad-PC-Pad liposomes under static condition (glass capillary) and under dynamic conditions as a function the microfluidic device positions displayed in the sketch of Fig. 5.

Flow rate[μL/s]	Glass capillary	R_g [nm]						
		Microfluidic device positions						
		#1	#2	A	#3	B	#4	#5
0	60.3±0.4							
0.002		59.5±0.2	59.1±0.1	60.3±0.4	63.0±0.5	59.3±0.9	61.1±0.2	61.6±0.2
0.02		60.2±0.2	58.0±0.4	55.1±0.5	64.3±0.6	52.4±0.8	59.1±0.3	61.3±0.1
0.20		61.6±0.4	61.0±0.5	61.4±0.6	64.0±0.8	52.3±0.9	58.0±0.3	60.0±0.4

The data represent the mean values of the normal distribution, including the associated errors derived from the standard deviation.

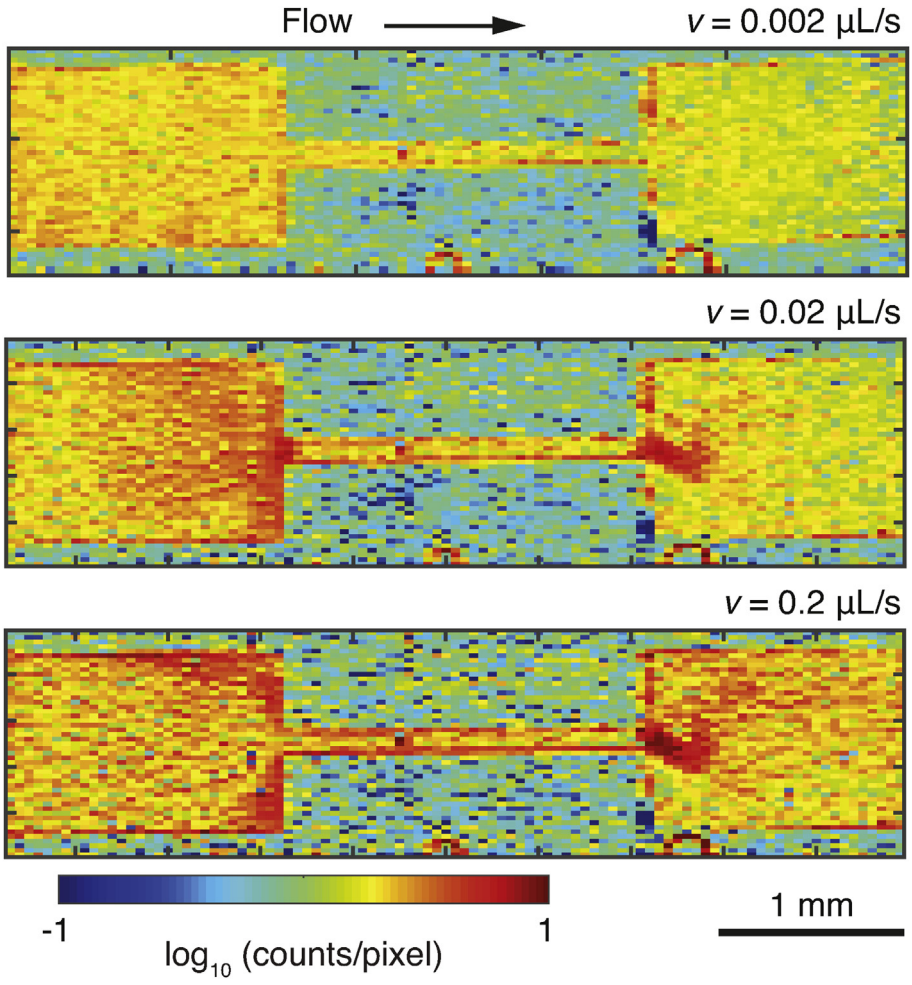

Fig. 4. 2D maps of the average scattered intensity at three flow rates v in the q-range from 0.096 to 0.102 nm. At the flow rate $v = 0.002$ μL/s, the intensity appears rather homogeneous on both sides of the constriction, albeit slightly higher intensity is registered on the inlet side. At higher flow rates ($v = 0.02$, 0.2 μL/s), a signal of increased intensity with a distinct plume-like shape is visible immediately at the constriction exit, whereas at the constriction entrance, the signal reveals high intensity at the intermediate flow rate and reduced intensity with stagnation zones at the device walls at the highest flow rate. 2D, two-dimensional.

Ref. [45], if one includes the calculated standard deviations $2\sigma = 3.0$ nm over the two phospholipid heads.

To fit the form factor related to the overall shape of Pad-PC-Pad, a thin ellipsoidal shell model was used [40]. An eccentricity ε of 0.43 was found, in agreement with the value reported in Ref. [11]. As for DPPC/DSPE-PEG, the intensity peak related to the interdigitated bilayer thickness d_{id} was fitted using a function for a bilayer with a Gaussian electron density profile [41,42] and a normal distribution over d_{id}. The results showed a mean value of $d_{id} = 3.3$ nm and standard deviation of $2\sigma = 1.4$ nm over the two phospholipid heads.

At low q-values of Pad-PC-Pad scattering curve, the Guinier approximation [46] was used to determine the radius of gyration (R_g) and found $R_g = 60.3$ nm with standard deviation $\sigma_{R_g} = 0.4$ nm (see Table 2), in line with the averaged diameter value obtained from the DLS (131.6 nm).

3.3. SAXS measurements of Pad-PC-Pad under dynamic conditions

The measurement in glass capillaries provided the fingerprint of Pad-PC-Pad liposome structure in static condition. In order to investigate the behavior of Pad-PC-Pad liposomes under an external perturbation, such as a shear stress gradient, 2D raster SAXS scans of Pad-PC-Pad liposomes under flow conditions, produced in a microfluidic device, were recorded. The present study relies on one microfluidic device. Hence, the observed structural changes are caused by the flow modifications.

Three flow velocities v were tested: $v = 0.002$, 0.02, and 0.2 μL/s. The corresponding shear rates were determined using Eq. (1). From the lowest to the highest flow rate, the shear rates in the constriction ($h = 250$ μm, $w = 125$ μm) were $\gamma = 1.54$, 15.4, and 154.0 s^{-1}, whereas in the wide region ($h = 250$ μm, $w = 1000$ μm), they corresponded to $\gamma = 0.2$ s^{-1}, 2.0 s^{-1}, and 20.0 s^{-1}.

2D maps of the mean scattering intensity in the range $\Delta q = 0.096$ to 0.102 nm^{-1} corresponding to a real space range $\Delta d = 65.4$ to 61.6 nm between the overall size and the size of the phospholipid head-to-head distance are shown in Fig. 4.

The non-symmetric intensity distribution observed in the 2D maps is indicative of the complex behavior of the liposomes under varying flow conditions, and it is apparent that the flow rate, and as a consequence, the shear stress, affects the liposomes, giving rise to variations in scattering signal depending on the location within the device. At the lowest flow rate, slightly increased intensity on the inlet side was observed.

At the intermediate flow rate, the constriction significantly changed the flow field, which accelerated approaching the constriction, diverged in a plume-like shape immediately after the constriction, and finally decelerated far from the constriction. Surprisingly, within the constriction and for the whole length of it, the scattering signal decreased with respect to its entrance.

For the highest flow rate, a similar behavior was observed, with the difference that the intensity distribution at the inlet was 'inverted', i.e. stronger along the device walls. This stronger intensity at the device walls is indicative of a stagnation zone, which was already incipient at the intermediate flow rate. Immediately after the constriction, a high-intensity 'plume' akin to that at the intermediate flow rate was observed.

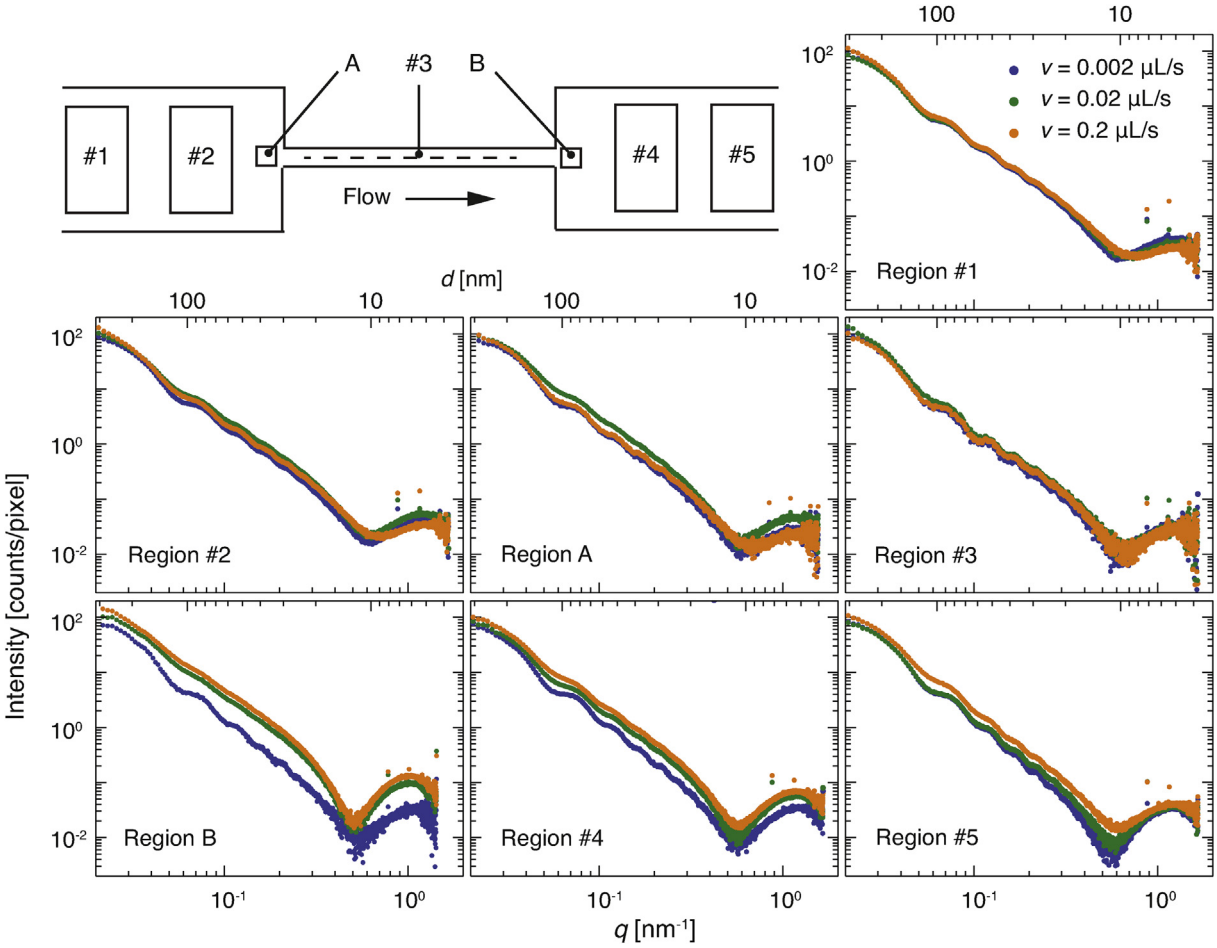

Fig. 5. Top left, sketch of the microfluidic device showing the seven regions selected. For each region, the radially integrated scattering signal is plotted for the three flow rates ($v = 0.002$ μL/s in blue, $v = 0.02$ μL/s in green, and $v = 0.2$ μL/s in orange). Differences at high q-values are apparent in the regions before and after constriction, indicating changes in bilayer thickness, and are pronounced at higher flow rates.

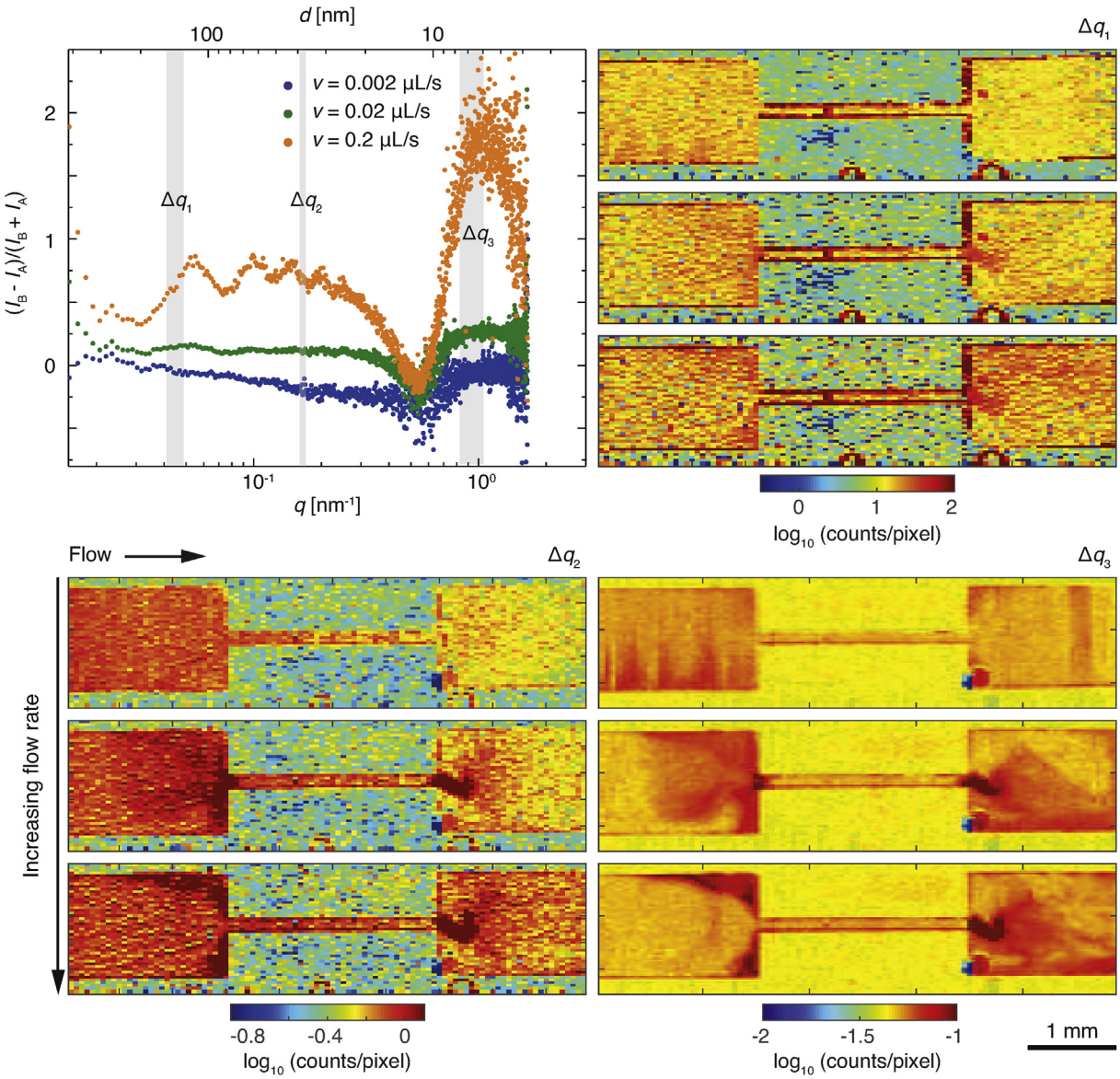

Fig. 6. The graph shows the normalized difference $(I_B - I_A)/(I_B + I_A)$ of the I *vs.* q curves in regions A and B (*cf.* Fig. 5) for the three flow rates. Especially for the highest flow rate, marked differences are seen in scattering signal, prominently at high q, indicating changes in head-to-head distance. 2D maps of average scattered intensity are shown for three selected q-ranges ($\Delta q_1 = 0.04$ to 0.05 nm^{-1}, $\Delta q_2 = 0.16$ to 0.17 nm^{-1}, and $\Delta q_3 = 0.83$ to 1.12 nm^{-1}). As in Fig. 4, the establishment of a flow field with an increasing flow rate can be observed. 2D, two-dimensional.

The local modifications of the averaged scattering intensity distribution observed in the 2D scanning SAXS maps of Fig. 4 supported the selection of seven regions of the microfluidic device, as shown in the sketch of Fig. 5. Three regions were selected before the constriction: one far (#1), one approaching (#2), and one very close (A); symmetrically, on the outlet side, three areas were chosen: one very close (B), one close (#4), and one far from the constriction (#5). Region #3 was selected in the constriction avoiding the edges of the device. For each region, the radially integrated scattering intensity I as a function of the scattering vector q at each flow rate v is shown.

On the inlet side (regions #1 and #2), no significant change at low and medium q can be observed as a function of v.

The oscillations of $I(q)$ observed at medium q overlap, indicating similar shape and size distributions of the liposomes. In contrast, the mean bilayer thickness slightly decreased with increasing flow, indicated by the shift of the position of the minimum to higher q (see Table 1).

In region A at the lowest flow rate, the scattering signal was comparable to the one observed in regions #1 and #2 at all q-ranges. At the intermediate flow rate and at intermediate q, the oscillations smeared out. The smearing might indicate a change in the overall shape of the liposomes.

At $v = 0.2$ μL/s, the oscillation appeared again more pronounced, similar to the lowest flow rate, and the position of the minimum shifted to the right, in line with a decrease of the mean bilayer thickness.

Within the constriction (region #3), the scattering curves of the liposomes did not display any significant difference by varying the flow rate. However, an increase of the R_g values was observed at the three flow rates (see Table 2) with respect to the static condition and the regions before the constriction. No significant change in the mean bilayer thickness values was detected. It should, however, be noted that the signal from the constriction is less reliable because of residual edge scattering from the device walls.

At the constriction exit (region B), the oscillations, still pronounced at the lowest flow rate, smeared out completely at the intermediate and high flow rate. In fact, the R_g values reported in Table 2 were comparable to the value found under static condition but showed a decrease of about

13% at a higher flow rate. Furthermore, the minimum shifted to lower q values, from 0.50 to 0.45 nm^{-1} indicating that in this region, the flow field caused an increase of the mean bilayer thickness of about 30% compared to the static condition (see Table 1).

The experimentally derived bilayer thickness increase by about 30% is an average value. It is interpreted as the loss of interdigitation, cf. Fig. 1. The authors hypothesize that the interdigitated membranes are tight, whereas the non-interdigitated membranes are leaky. Therefore, the faceted Pad-PC-Pad liposomes are tight at rest and become leaky through mechanical stimulation.

The increase of the bilayer thickness of Pad-PC-Pad is in line with a mechanically induced loss of full interdigitation of phospholipid amide chains, which is usually observed at the liquid-crystalline phase (above the transition temperature) and, in presence of cholesterol, at the gel phase (below the transition temperature) [47].

In region #4, the scattering signal gradually reduced.

For the intermediate and high flow rates, the oscillations were smeared, as in region B, whereas for the lowest flow rate, the oscillations were well visible, as in region #2. The position of the minimum did not vary significantly among the three flow rates, indicating no significant modification on the bilayer thickness.

In region #5 and at the three flow rates, the oscillations appeared similar as in region #1. In contrast, the position of the minimum, at the highest flow rate, shifted slightly to the right, from 0.55 to 0.6 nm^{-1}, compared to the intermediate and lowest flow rate.

Owing to the impact of the local flow field, alteration of the liposome morphology in regions A and B was detected (see Fig. 5), both at the high and low q, compared to the other regions where modifications, by varying the flow rate, were observed either at low q (e.g., region #5) or at high q (e.g., regions #1 and #2).

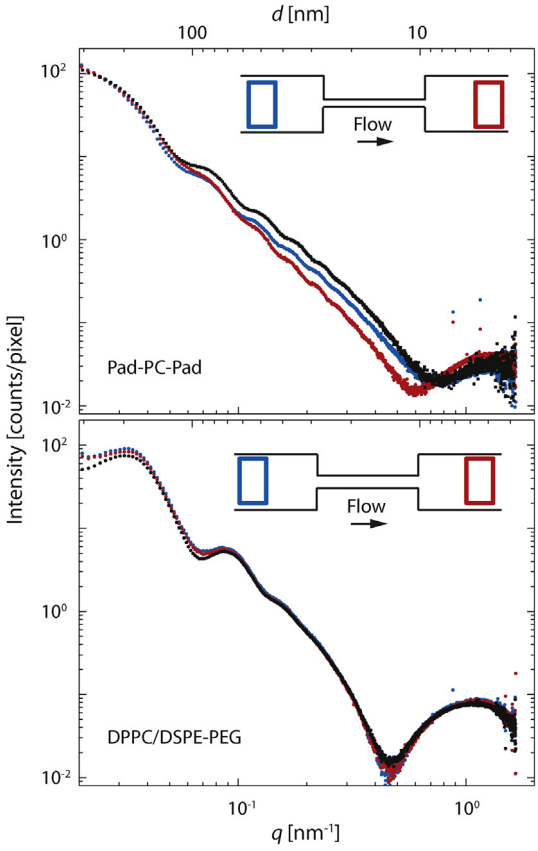

Fig. 7. Comparison of the scattering intensity curves for the same maximum shear acting on Pad-PC-Pad (top) and DPPC/DSPE-PEG (bottom) before (blue-colored dots) and after (red-colored dots) constriction. A significant shift of the bilayer peak of Pad-PC-Pad liposomes is observed after the constriction with respect to the scattering signal before the constriction and under static condition (dark-colored dots). DPPC, 1,2-dipalmitoyl-*sn*-glycero-3-phosphatidylcholine.

To highlight the changes of regions A (before constriction) and B (after constriction) at the three flow rates (see Fig. 5), the scattering curves in these two regions were displayed as normalized difference of their scattering intensities (see graph in Fig. 6).

Herein, three Δq ranges were selected, including the mean overall size of the liposomes ($\Delta q_1 = 0.04 - 0.05\ nm^{-1}$), the size around the bilayer thickness ($\Delta q_3 = 0.83 - 1.12\ nm^{-1}$), and a range in between ($\Delta q_2 = 0.16 - 0.17\ nm^{-1}$). 2D maps of the integrated scattered intensity in each selected Δq at each flow rate are displayed.

The 2D map at the lowest flow rate and in the range Δq_3 (see Fig. 6, bottom right) showed vertical stripes before and after the constriction, clear sign of the presence of artifacts within the microfluidic device. At the three Δq ranges selected, the 2D maps (see Fig. 6) and a trend comparable to the one shown in Fig. 4 were observed.

The response of Pad-PC-Pad liposomes to the flow field was compared with the one of DPPC/DSPE-PEG as reported in Fig. 7. Herein, the scattering signals of Pad-PC-Pad and DPPC/DSPE-PEG were radially integrated in the two areas—blue and red boxes—indicated in the device sketches of Fig. 7.

DPPC/DSPE-PEG measurements in dynamic conditions were carried out in a microfluidic device having a constriction width two times wider ($w_{constriction} = 250\ \mu m$) than the one utilized for Pad-Pad-Pad. For a fair comparison, and considering Eq. (1), the same shear condition at the constriction location was obtained by setting twice the flow rate for DPPC/DSPE-PEG liposomes than the flow rate to which Pad-PC-Pad liposomes were subjected.

Significant differences in scattering curves, including the shift of the bilayer peak, from the SAXS signals of Pad-PC-Pad liposomes before and after the constriction are present, whereas no changes of DPPC/DSPE-PEG liposomes could be probed as their scattering signals under static condition and under dynamic conditions (before and after the constriction) overlapped. The comparison with DPPC/DSPE-PEG liposomes supports our hypothesis that Pad-PC-Pad liposomes are mechanoresponsive, already before the constriction and at the shear rates here investigated.

4. Conclusions

The combination of microfluidics and spatially resolved SAXS allows for the *in situ* and real-time detection of flow-induced structural modifications of three-dimensional nanostructures on the entire nanometer scale, as exemplarily demonstrated for Pad-PC-Pad liposomes with a broad variety of shapes. The fact that the Pad-PC-Pad liposomes change their shape and bilayer thickness before reaching the constriction clearly indicates the presence of an additional phenomenon. Simple estimations on the shear and the gradient pressure forces acting on the liposomes show comparable maximal amplitudes. Although the shear stress is highest at the wall along the stenosis, the pressure gradients occur at inlets and outlets of the constriction. Consequently, the localization enables us to discriminate between the two physical phenomena. The unique approach also permits the investigation of shear rates outside the physiological range. In this study, three flow rates were selected, which are well below the maximal values during the pulsatile flow in healthy and stenotic blood vessels. Nonetheless, the liposomes responded to the mechanical stimuli. Therefore, one can reasonably assume that the present publication will initiate a flood of biomedical studies on mechanically induced drug release from non-spherical liposomes with interdigitated lipid bilayers. The combination of microfluidics and spatially resolved SAXS, however, is not only vital for the understanding of efficient drug release from faceted liposomes but may become relevant for other soft matter systems of nanometer size.

Conflicts of interest

The authors declare that they have no known competing financial

interests or personal relationships that could have appeared to influence the work reported in this paper.

Acknowledgments

This work was partially funded by the Swiss National Science Foundation (SNSF) project 126090 via the National Research Program (NRP) 62 'Smart Materials'. The authors thank Sofiya Matviykiv for support during liposome preparation, Dennis Mueller for Pad-PC-Pad lipid synthesis, and Viviane Lutz Bueno for valuable discussion on microfluidic devices and support on masters fabrication. The authors thank Marianne Liebi for support during the experiment carried out at the cSAXS beamline (proposal 20151414). The valuable service of Takashi Ishikawa (Paul Scherrer Institute, Switzerland) in collecting the micrograph (Fig. 2) at PSI EM Facility is gratefully acknowledged.

References

[1] G. Lanza, P. Winter, T. Cyrus, S. Caruthers, J. Marsh, M. Hughes, S. Wickline, Nanomedicine opportunities in cardiology, Ann. N. Y. Acad. Sci. 1080 (2006) 451–465.
[2] W. Yin, S.K. Shanmugavelayudam, D.A. Rubenstein, 3D numerical simulation of coronary blood flow and its effect on endothelial cell activation, in: Engineering in Medicine and Biology Society. Annual International Conference of the IEEE, 2009, pp. 4003–4006.
[3] M.N. Holme, I.A. Fedotenko, D. Abegg, J. Althaus, L. Babel, F. Favarger, R. Reiter, R. Tanasescu, P.-L. Zaffalon, A. Ziegler, B. Müller, T. Saxer, A. Zumbuehl, Shear-stress sensitive lenticular vesicles for targeted drug delivery, Nat. Nanotechnol. 7 (2012) 536–543.
[4] N. Korin, M. Kanapathipillai, B.D. Matthews, M. Crescente, A. Brill, T. Mammoto, K. Ghosh, S. Jurek, S.A. Bencherif, D. Bhatta, A.U. Coskun, C.L. Feldman, D.D. Wagner, D.E. Ingber, Shear-activated nanotherapeutics for drug targeting to obstructed blood vessels, Science 337 (2012) 738–742.
[5] S. Tinkle, S.E. McNeil, S. Mühlebach, R. Bawa, G. Borchard, Y.C. Barenholz, L. Tamarkin, N. Desai, Nanomedicines: addressing the scientific and regulatory gap, Ann. N. Y. Acad. Sci. 1313 (2014) 35–56.
[6] V.P. Torchilin, Recent advances with liposomes as pharmaceutical carriers, Nat. Rev. Drug Discov. 4 (2005) 145–160.
[7] I.A. Fedotenko, P.-L. Zaffalon, F. Favarger, A. Zumbuehl, The synthesis of 1,3-diamidophospholipids, Tetrahedron Lett. 51 (2010) 5382–5384.
[8] M. Dubois, T. Zemb, Swelling limits for bilayer microstructures: the implosion of lamellar structure versus disordered lamellae, Curr. Opin. Colloid Interface Sci. 5 (2000) 27–37.
[9] A. Weinberger, R. Tanasescu, C. Stefaniu, l. A. Fedotenko, F. Favarger, T. Ishikawa, G. Brezesinski, C.M. Marques, A. Zumbuehl, Bilayer properties of 1,3-Diamidophospholipids, Langmuir 31 (2015) 1879–1884.
[10] S. Bugna, M. Buscema, S. Matviykiv, R. Urbanics, A. Weinberger, T. Meszaros, J. Szebeni, A. Zumbuehl, T. Saxer, B. Müller, Surprising lack of liposome-induced complement activation by artificial 1,3-diamidophospholipids in vitro, Nanomed. Nanotechnol. Biol. Med. 12 (2016) 845–849.
[11] M. Buscema, et al., Immunological response to nitroglycerin-loaded shear-responsive liposomes in vitro and in vivo, J. Control. Release 264 (2017) 14–23.
[12] M. Hope, M. Bally, G. Webb, P. Cullis, Production of large unilamellar vesicles by a rapid extrusion procedure. Characterization of size distribution, trapped volume and ability to maintain a membrane potential, Biochim. Biophys. Acta Biomembr. 812 (1985) 55–65.
[13] S.U. Engelhaaf, B. Wehrli, M. Müller, M. Adrian, P. Schurtenberger, Determination of the size distribution of lecithin liposomes: a comparative study using freeze fracture, cryoelectron microscopy and dynamic light scattering, J. Microsc. 184 (1996) 214–228.
[14] S. Helvig, I.D. Azmi, S.M. Moghimi, A. Yaghmur, Recent advances in cryo-TEM imaging of soft lipid nanoparticles, AIMS Biophysics 2 (2015) 116–130.
[15] O. Et-Thakafy, N. Delorme, F. Guyomarc'h, C. Lopez, Mechanical properties of milk sphingomyelin bilayer membranes in the gel phase: effects of naturally complex heterogeneity, saturation and acyl chain length investigated on liposomes using AFM, Chem. Phys. Lipids 210 (2018) 47–59.
[16] R. Garcia-Diez, C. Gollwitzer, M. Krumrey, Z. Varga, Size determination of a liposomal drug by small-angle X-ray scattering using continuous contrast variation, Langmuir 32 (2016) 772–778.
[17] F. Foglia, A. Drake, A. Terry, S. Rogers, M. Lawrence, D. Barlow, Small-angle neutron scattering studies of the effects of amphotericin B on phospholipid and phospholipid-sterol membrane structure, Biochim. Biophys. Acta (BBA) Biomembranes 1808 (2011) 1574–1580.
[18] S. Köster, T. Pfohl, X-ray studies of biological matter in microfluidic environments, Mod. Phys. Lett. B 26 (2012) 1230018.
[19] O. Bunk, M. Bech, T.H. Jensen, R. Feidenhans'l, T. Binderup, A. Menzel, F. Pfeiffer, Multimodal x-ray scatter imaging, New J. Phys. 11 (2009) 123016.
[20] B. Müller, H. Deyhle, D.A. Bradley, M. Farquharson, G. Schulz, M. Müller-Gerbl, O. Bunk, Nanomethods: scanning X-ray scattering: evaluating the nanostructure of human tissues, Eur. J. Nanomed. 3 (2010) 30–33.
[21] S. Gaiser, H. Deyhle, O. Bunk, S.N. White, B. Müller, Understanding nano-anatomy of healthy and carious human teeth: a prerequisite for nanodentistry, Biointerphases 7 (2012) 4.
[22] M. Georgiadis, M. Guizar-Sicairos, A. Zwahlen, A.J. Trüssel, O. Bunk, R. Müller, P. Schneider, 3D scanning SAXS: a novel method for the assessment of bone ultrastructure orientation, Bone 71 (2015) 42–52.
[23] V. Lutz-Bueno, J. Zhao, R. Mezzenga, T. Pfohl, P. Fischer, M. Liebi, Scanning-SAXS of microfluidic flows: nanostructural mapping of soft matter, Lab Chip 16 (2016) 4028–4035.
[24] N. Pham, D. Radajewski, A. Round, M. Brennich, P. Pernot, B. Biscans, F. Bonneté, S. Teychene, Coupling high throughput microfluidics and small-angle X-ray scattering to study protein crystallization from solution, Anal. Chem. 89 (2017) 2282–2287.
[25] T.A. Balbino, A.R. Azzoni, L.G. de la Torre, Microfluidic devices for continuous production of pDNA/cationic liposome complexes for gene delivery and vaccine therapy, Colloids Surfaces B Biointerfaces 111 (2013) 203–210.
[26] L. Pollack, M.W. Tate, N.C. Darnton, J.B. Knight, S.M. Gruner, W.A. Eaton, R.H. Austin, Compactness of the denatured state of a fast-folding protein measured by submillisecond small-angle x-ray scattering, Proc. Natl. Acad. Sci. Unit. States Am. 96 (1999) 10115–10117.
[27] A.C. Toma, R. Dootz, T. Pfohl, Analysis of complex fluids using microfluidics: the particular case of DNA/polycations assemblies, J. Phys. D Appl. Phys. 46 (2013) 114001.
[28] A.S. Poulos, M. Nania, P. Lapham, R.M. Miller, A.J. Smith, H. Tantawy, J. Caragay, J. Gummel, O. Ces, E.S.J. Robles, J.T. Cabral, Microfluidic SAXS study of lamellar and multilamellar vesicle phases of linear sodium alkylbenzenesulfonate surfactant with intrinsic isomeric distribution, Langmuir 32 (2016) 5852–5861.
[29] S. With, M. Trebbin, C.B.A. Bartz, C. Neuber, M. Dulle, S. Yu, S.V. Roth, H.-W. Schmidt, S. Förster, Fast diffusion-limited lyotropic phase transitions studied in situ using continuous flow microfluidics/microfocus-SAXS, Langmuir 30 (2014) 12494–12502.
[30] R. Dootz, H. Evans, S. Köster, T. Pfohl, Rapid prototyping of X-ray microdiffraction compatible continuous microflow foils, Small 3 (2007) 96–100.
[31] C.P. Molloy, Y. Yao, H. Kammoun, T. Bonnard, T. Hoefer, K. Alt, F. Trovar-Lopez, G. Rosengarten, P.A. Ramsland, A.D. Meer, A. Berg, A.J. Murphy, C.E. Hagemeyer, K. Peter, E. Westein, Shear-sensitive nanocapsule drug release for site- specific inhibition of occlusive thrombus formation, J. Thromb. Haemost. 15 (2016) 972–982.
[32] N. Venugopal Menon, H.M. Tay, K.T. Pang, R. Dalan, S.C. Wong, X. Wang, K.H.H. Li, H.W. Hou, A tunable microfluidic 3D stenosis model to study leukocyte-endothelial interactions in atherosclerosis, APL Bioengineering 2 (2018), 016103.
[33] D. Mellal, A. Zumbuehl, Exit-strategies–smart ways to release phospholipid vesicle cargo, J. Mater. Chem. B 2 (2014) 247–252.
[34] P. Walde, Preparation of vesicles (liposomes), Encycl. Nanosci. Nanotechnol. 9 (2004) 43–79.
[35] F. Olson, C. Hunt, F. Szoka, W. Vail, D. Papahadjopoulos, Preparation of liposomes of defined size distribution by extrusion through polycarbonate membranes, Biochimica et Biophysica Acta (BBA) - Biomembranes 557 (1979) 9–23.
[36] E. Stalder, A. Zumbuehl, Phosphate test 2.0, CHIMIA International Journal for Chemistry 67 (2013) 819–821.
[37] P. Kraft, A. Bergamaschi, C. Broennimann, R. Dinapoli, E.F. Eikenberry, B. Henrich, I. Johnson, A. Mozzanica, C.M. Schlepütz, P.R. Willmott, B. Schmitt, Performance of single-photon-counting PILATUS detector modules, J. Synchrotron Radiat. 16 (2009) 368–375.
[38] V. Vasilca, A. Sadeghpour, S. Rawson, L. Hawke, S. Baldwin, T. Wilkinson, D. Bannister, V. Postis, M. Rappolt, S. Muench, L. Jeukena, Spherical-supported membranes as novel platforms for the screening of membrane protein targets, Anal. Biochem. 549 (2018) 58–65.
[39] G. Porod, Die Abhangigkeitder Rontgen-Kleinwinkelstreuung von Form und Grösse der kolloiden Teilchen in verdünnten Systemen, IV, Acta Phys. Austriaca 2 (1948) 255–292.
[40] I. Breßler, J. Kohlbrecher, A.F. Thünemann, SASfit: a tool for small-angle scattering data analysis using a library of analytical expressions, J. Appl. Crystallogr. 48 (2015) 1587–1598.
[41] G. Pabst, R. Koschuch, B. Pozo-Navas, M. Rappolt, K. Lohner, P. Laggner, Structural analysis of weakly ordered membrane stacks, J. Appl. Crystallogr. 36 (2003) 1378–1388.
[42] G. Pabst, M. Rappolt, H. Amenitsch, P. Laggner, Structural information from multilamellar liposomes at full hydration: full q-range fitting with high quality x-ray data, Phys. Rev. 62 (2000) 4000.
[43] O. Glatter, O. Kratky, Small Angle X-Ray Scattering, Academic press, 1982.
[44] G. Bozzuto, A. Molinari, Liposomes as nanomedical devices, Int. J. Nanomed. 10 (2015) 975–999.
[45] M. Wang, T. Zander, X. Liu, C. Liu, A. Raj, D.F. Wieland, V.M. Garamus, R. Willumeit-Römer, P.M. Claesson, A. Dedinaite, The effect of temperature on supported dipalmitoylphosphatidylcholine (DPPC) bilayers: structure and lubrication performance, J. Colloid Interface Sci. 445 (2015) 84–92.
[46] A. Guinier, La diffraction des rayons X aux très petits angles: application à l'étude de phénomènes ultramicroscopiques, Ann. Phys. 11 (1939) 161–237.
[47] R. Tanasescu, M.A. Lanz, D. Mueller, S. Tassler, T. Ishikawa, R. Reiter, G. Brezesinski, A. Zumbuehl, Vesicle origami and the influence of cholesterol on lipid packing, Langmuir 32 (2016) 4896–4903.